

Experimental access to Transition Distribution Amplitudes with the PANDA experiment at FAIR

The PANDA Collaboration

B.P. Singh¹, W. Erni², I. Keshelashvili², B. Krusche², M. Steinacher², B. Liu³, H. Liu³, Z. Liu³, X. Shen³, C. Wang³, J. Zhao³, M. Albrecht⁴, M. Fink⁴, F.H. Heinsius⁴, T. Held⁴, T. Holtmann⁴, H. Koch⁴, B. Kopf⁴, M. Kümmel⁴, G. Kuhl⁴, M. Kuhlmann⁴, M. Leyhe⁴, M. Mikirtychyants⁴, P. Musiol⁴, A. Mustafa⁴, M. Pelizäus⁴, J. Pychy⁴, M. Richter⁴, C. Schnier⁴, T. Schröder⁴, C. Sowa⁴, M. Steinke⁴, T. Triffterer⁴, U. Wiedner⁴, R. Beck⁵, C. Hammann⁵, D. Kaiser⁵, B. Ketzer⁵, M. Kube⁵, P. Mahlberg⁵, M. Rossbach⁵, C. Schmidt⁵, R. Schmitz⁵, U. Thoma⁵, D. Walther⁵, C. Wendel⁵, A. Wilson⁵, A. Bianconi⁶, M. Bragadireanu⁷, M. Caprini⁷, D. Pantea⁷, D. Pietreanu⁷, M.E. Vasile⁷, B. Patel⁸, D. Kaplan⁹, P. Brandys¹⁰, T. Czyzewski¹⁰, W. Czyzycki¹⁰, M. Domagala¹⁰, M. Hawryluk¹⁰, G. Filo¹⁰, M. Krawczyk¹⁰, D. Kwiatkowski¹⁰, E. Lisowski¹⁰, F. Lisowski¹⁰, T. Fiutowski¹¹, M. Idzik¹¹, B. Mindur¹¹, D. Przyborowski¹¹, K. Swientek¹¹, B. Czech¹², S. Kliczewski¹², K. Korcyl¹², A. Kozela¹², P. Kulesa¹², P. Lebedowicz¹², K. Malgorzata¹², K. Pysz¹², W. Schäfer¹², R. Siudak¹², A. Szczurek¹², J. Biernat¹³, S. Jowzaee¹³, B. Kamys¹³, S. Kistryn¹³, G. Korcyl¹³, W. Krzemien¹³, A. Magiera¹³, P. Moskal¹³, M. Palka¹³, A. Pszytniak¹³, Z. Rudy¹³, P. Salabura¹³, J. Smyrski¹³, P. Strzempek¹³, A. Wrońska¹³, I. Augustin¹⁴, I. Lehmann¹⁴, D. Nicmorus¹⁴, G. Schepers¹⁴, L. Schmitt¹⁴, M. Al-Turany¹⁵, U. Cahit¹⁵, L. Capozza¹⁵, A. Dbeyssi¹⁵, H. Deppe¹⁵, R. Dzhygadlov¹⁵, A. Ehret¹⁵, H. Flemming¹⁵, A. Gerhardt¹⁵, K. Götzen¹⁵, R. Karabowicz¹⁵, R. Kliemt¹⁵, J. Kunkel¹⁵, U. Kurilla¹⁵, D. Lehmann¹⁵, J. Lühning¹⁵, F. Maas¹⁵, C. Morales Morales¹⁵, M.C. Mora Espi¹⁵, F. Nerling¹⁵, H. Orth¹⁵, K. Peters¹⁵, D. Rodríguez Piñeiro¹⁵, N. Saito¹⁵, T. Saito¹⁵, A. Sánchez Lorente¹⁵, C.J. Schmidt¹⁵, C. Schwarz¹⁵, J. Schwiening¹⁵, M. Traxler¹⁵, R. Valente¹⁵, B. Voss¹⁵, P. Wieczorek¹⁵, A. Wilms¹⁵, M. Zühlsdorf¹⁵, V.M. Abazov¹⁶, G. Alexeev¹⁶, A. Arefiev¹⁶, V.I. Astakhov¹⁶, M.Yu. Barabanov¹⁶, B.V. Batyunya¹⁶, Yu.I. Davydov¹⁶, V.Kh. Dodokhov¹⁶, A.A. Efremov¹⁶, A.G. Fedunov¹⁶, A.A. Festchenko¹⁶, A.S. Galoyan¹⁶, S. Grigoryan¹⁶, A. Karmokov¹⁶, E.K. Koshurnikov¹⁶, V.I. Lobanov¹⁶, Yu.Yu. Lobanov¹⁶, A.F. Makarov¹⁶, L.V. Malinina¹⁶, V.L. Malyshev¹⁶, G.A. Mustafaev¹⁶, A. Olshevskiy¹⁶, M.A. Pasyuk¹⁶, E.A. Perevalova¹⁶, A.A. Piskun¹⁶, T.A. Pocheptsov¹⁶, G. Pontecorvo¹⁶, V.K. Rodionov¹⁶, Yu.N. Rogov¹⁶, R.A. Salmin¹⁶, A.G. Samartsev¹⁶, M.G. Sapozhnikov¹⁶, G.S. Shabratova¹⁶, N.B. Skachkov¹⁶, A.N. Skachkova¹⁶, E.A. Stokovsky¹⁶, M.K. Suleimanov¹⁶, R.Sh. Teshev¹⁶, V.V. Tokmenin¹⁶, V.V. Uzhinsky¹⁶, A.S. Vodopyanov¹⁶, S.A. Zaporozhets¹⁶, N.I. Zhuravlev¹⁶, A.G. Zorin¹⁶, D. Branford¹⁷, D. Glazier¹⁷, D. Watts¹⁷, P. Woods¹⁷, A. Britting¹⁸, W. Eylich¹⁸, A. Lehmann¹⁸, F. Uhlig¹⁸, S. Dobbs¹⁹, K. Seth¹⁹, A. Tomaradze¹⁹, T. Xiao¹⁹, D. Bettoni²⁰, V. Carassiti²⁰, A. Cotta Ramusino²⁰, P. Dalpiaz²⁰, A. Drago²⁰, E. Fioravanti²⁰, I. Garzia²⁰, M. Savriè²⁰, G. Stancari²⁰, V. Akishina²¹, I. Kisel²¹, I. Kulakov²¹, M. Zyzak²¹, R. Arora²², T. Bei²², A. Gromliuk²², G. Kalicy²², M. Krebs²², M. Patsyuk²², M. Zuehlsdorf²², N. Bianchi²³, P. Gianotti²³, C. Guaraldo²³, V. Lucherini²³, E. Pace²³, A. Bersani²⁴, G. Bracco²⁴, M. Macri²⁴, R.F. Parodi²⁴, S. Bianco²⁵, D. Bremer²⁵, K.T. Brinkmann²⁵, S. Diehl²⁵, V. Dormenev²⁵, P. Drexler²⁵, M. Düren²⁵, T. Eissner²⁵, E. Etzelmueller²⁵, K. Föhl²⁵, M. Galuska²⁵, T. Gessler²⁵, E. Gutz²⁵, A. Hayrapetyan²⁵, J. Hu²⁵, B. Kröck²⁵, W. Kühn²⁵, T. Kuske²⁵, S. Lange²⁵, Y. Liang²⁵, O. Merle²⁵, V. Metag²⁵, D. Mühlheim²⁵, D. Münchow²⁵, M. Nanova²⁵, R. Novotny²⁵, A. Pitka²⁵, T. Quagli²⁵, J. Rieke²⁵, C. Rosenbaum²⁵, R. Schnell²⁵, B. Spruck²⁵, H. Stenzel²⁵, U. Thöring²⁵, T. Ullrich²⁵, T. Wasem²⁵, M. Werner²⁵, H.G. Zaunick²⁵, D. Ireland²⁶, G. Rosner²⁶, B. Seitz²⁶, P.N. Deepak²⁷, A.V. Kulkarni²⁷, A. Apostolou²⁸, M. Babai²⁸, M. Kavatsyuk²⁸, P. Lemmens²⁸, M. Lindemulder²⁸, H. Löhner²⁸, J. Messchendorp²⁸, P. Schakel²⁸, H. Smit²⁸, J.C. van der Wee²⁸, R. Veenstra²⁸, M. Tiemens²⁸, S. Vejdani²⁸, K. Kalita²⁹, D.P. Mohanta²⁹, A. Kumar³⁰, A. Roy³⁰, R. Sahoo³⁰, H. Sohlbach³¹, M. Büscher³², L. Cao³², A. Cebulla³², D. Deermann³², R. Dosdall³², S. Esch³², I. Georgadze³², A. Gillitzer³², A. Goerres³², F. Goldenbaum³², D. Grunwald³², A. Herten³², Q. Hu³², G. Kemmerling³², H. Kleines³², V. Kozlov³², A. Lehrach³², S. Leiber³², R. Maier³², R. Nellen³², H. Ohm³², S. Orfanitski³², D. Prasuhn³², E. Prencipe³², J. Ritman³², S. Schadmand³², J. Schumann³², T. Sefzick³², V. Serdyuk³², G. Sterzenbach³², T. Stockmanns³², P. Wintz³², P. Wüstner³², H. Xu³², S. Li³³, Z. Li³³, Z. Sun³³, H. Xu³³, V. Rigato³⁴, S. Fissum³⁵, K. Hansen³⁵, L. Isaksson³⁵, M. Lundin³⁵, B. Schröder³⁵, P. Achenbach³⁶, S. Bleser³⁶, M. Cardinali³⁶, O. Corelli³⁶, M. Deiseroth³⁶, A. Denig³⁶, M. Distler³⁶, F. Feldbauer³⁶, M. Fritsch³⁶, P. Jasinski³⁶, M. Hoek³⁶, D. Kangh³⁶, A. Karavdina³⁶, W. Lauth³⁶, H. Leithoff³⁶, H. Merkel³⁶, M. Michel³⁶, C. Motzko³⁶, U. Müller³⁶, O. Noll³⁶, S. Plueger³⁶, J. Pochodzalla³⁶, S. Sanchez³⁶, S. Schlimme³⁶, C. Sfienti³⁶, M. Steinen³⁶, M. Thiel³⁶, T. Weber³⁶,

M. Zambrana^{36 a}, V.I. Dormenev³⁷, A.A. Fedorov³⁷, M.V. Korzhik³⁷, O.V. Missevitch³⁷, P. Balanutsa³⁸, V. Balanutsa³⁸, V. Chernetsky³⁸, A. Demekhin³⁸, A. Dolgolenko³⁸, P. Fedorets³⁸, A. Gerasimov³⁸, V. Goryachev³⁸, V. Varentsov³⁸, A. Boukharov³⁹, O. Malyshev³⁹, I. Marishev³⁹, A. Semenov³⁹, I. Konorov⁴⁰, S. Paul⁴⁰, S. Grieser⁴¹, A.K. Hergemöller⁴¹, A. Khoukaz⁴¹, E. Köhler⁴¹, A. Täschner⁴¹, J. Wessels⁴¹, S. Dash⁴², M. Jadhav⁴², S. Kumar⁴², P. Sarin⁴², R. Varma⁴², V.B. Chandratre⁴³, V. Datar⁴³, D. Dutta⁴³, V. Jha⁴³, H. Kumawat⁴³, A.K. Mohanty⁴³, B. Roy⁴³, Y. Yan⁴⁴, K. Chinorat⁴⁴, K. Khanchai⁴⁴, L. Ayut⁴⁴, S. Pornrad⁴⁴, A.Y. Barnyakov⁴⁵, A.E. Blinov⁴⁵, V.E. Blinov^{45,46}, V.S. Bobrovnikov⁴⁵, S.A. Kononov^{45,47}, E.A. Kravchenko^{45,47}, I.A. Kuyanov⁴⁵, A.P. Onuchin^{45,46}, A.A. Sokolov^{45,47}, Y.A. Tikhonov^{45,47}, E. Atomssa⁴⁸, T. Hennino⁴⁸, M. Imre⁴⁸, R. Kunne⁴⁸, C. Le Galliard⁴⁸, B. Ma⁴⁸, D. Marchand⁴⁸, S. Ong⁴⁸, B. Ramstein⁴⁸, P. Rosier⁴⁸, E. Tomasi-Gustafsson⁴⁸, J. Van de Wiele⁴⁸, G. Boca⁴⁹, S. Costanza⁴⁹, P. Genova⁴⁹, L. Lavezzi⁴⁹, P. Montagna⁴⁹, A. Rotondi⁴⁹, V. Abramov⁵⁰, N. Belikov⁵⁰, S. Bukreeva⁵⁰, A. Davidenko⁵⁰, A. Derevschikov⁵⁰, Y. Goncharenko⁵⁰, V. Grishin⁵⁰, V. Kachanov⁵⁰, V. Kormilitzin⁵⁰, Y. Melnik⁵⁰, A. Levin⁵⁰, N. Minaev⁵⁰, V. Mochalov⁵⁰, D. Morozov⁵⁰, L. Nogach⁵⁰, S. Poslavskiy⁵⁰, A. Ryazantsev⁵⁰, S. Ryzhikov⁵⁰, P. Semenov⁵⁰, I. Shein⁵⁰, A. Uzunian⁵⁰, A. Vasiliev⁵⁰, A. Yakutin⁵⁰, B. Yabsley⁵¹, T. Bäck⁵², B. Cederwall⁵², K. Makónyi⁵³, P.E. Tegnér⁵³, K.M. von Würtemberg⁵³, S. Belostotski⁵⁴, G. Gavrilov⁵⁴, A. Izotov⁵⁴, A. Kashchuk⁵⁴, O. Levitskaya⁵⁴, S. Manaenkov⁵⁴, O. Miklukho⁵⁴, Y. Naryshkin⁵⁴, K. Suvorov⁵⁴, D. Veretennikov⁵⁴, A. Zhadanov⁵⁴, A.K. Rai⁵⁵, S.S. Godre⁵⁶, R. Duchat⁵⁶, A. Amoroso⁵⁷, A. Bianconi⁵⁷, M.P. Bussa⁵⁷, L. Busso⁵⁷, F. De Mori⁵⁷, M. Destefanis⁵⁷, L. Fava⁵⁷, L. Ferrero⁵⁷, M. Greco⁵⁷, M. Maggiora⁵⁷, G. Maniscalco⁵⁷, S. Marcello⁵⁷, S. Sosio⁵⁷, S. Spataro⁵⁷, L. Zotti⁵⁷, D. Calvo⁵⁸, S. Coli⁵⁸, P. De Remigis⁵⁸, A. Filippi⁵⁸, G. Giraudo⁵⁸, S. Lusso⁵⁸, G. Mazza⁵⁸, M. Mingnole⁵⁸, A. Rivetti⁵⁸, R. Wheadon⁵⁸, F. Balestra⁵⁹, F. Iazzi⁵⁹, R. Introzzi⁵⁹, A. Lavagno⁵⁹, H. Younis⁵⁹, R. Birsá⁶⁰, F. Bradamante⁶⁰, A. Bressan⁶⁰, A. Martin⁶⁰, H. Clement⁶¹, B. Gålnder⁶², L. Caldeira Balkeståhl⁶³, H. Calén⁶³, K. Fransson⁶³, T. Johansson⁶³, A. Kupsc⁶³, P. Marciniowski⁶³, J. Pettersson⁶³, K. Schönning⁶³, M. Wolke⁶³, J. Zlomanczuk⁶³, J. Díaz⁶⁴, A. Ortiz⁶⁴, P.C. Vinodkumar⁶⁵, A. Parmar⁶⁵, A. Chlopik⁶⁶, D. Melnychuk⁶⁶, B. Slowinski⁶⁶, A. Trzcinski⁶⁶, M. Wojciechowski⁶⁶, S. Wronka⁶⁶, B. Zwieglinski⁶⁶, P. Bühler⁶⁷, J. Marton⁶⁷, K. Suzuki⁶⁷, E. Widmann⁶⁷, J. Zmeskal⁶⁷

and

B. Fröhlich¹⁵, D. Khanef¹⁵, D. Lin¹⁵, I. Zimmermann¹⁵, and K. Semenov-Tian-Shansky⁶⁸

¹ Aligarth Muslim University, Physics Department, Aligarth India

² Universität Basel Switzerland

³ Institute of High Energy Physics, Chinese Academy of Sciences, Beijing China

⁴ Universität Bochum I. Institut für Experimentalphysik, Germany

⁵ Rheinische Friedrich-Wilhelms-Universität Bonn Germany

⁶ Università di Brescia Italy

⁷ Institutul National de C&D pentru Fizica si Inginerie Nucleara “Horia Hulubei”, Bukarest-Magurele Romania

⁸ P.D. Patel Institute of Applied Science, Department of Physical Sciences, Changa India

⁹ IIT, Illinois Institute of Technology, Chicago U.S.A.

¹⁰ University of Technology, Institute of Applied Informatics, Cracow Poland

¹¹ AGH, University of Science and Technology, Cracow Poland

¹² IFJ, Institute of Nuclear Physics PAN, Cracow Poland

¹³ Instytut Fizyki, Uniwersytet Jagiellonski, Cracow Poland

¹⁴ FAIR, Facility for Antiproton and Ion Research in Europe, Darmstadt Germany

¹⁵ GSI Helmholtzzentrum für Schwerionenforschung GmbH, Darmstadt Germany

¹⁶ Veksler-Baldin Laboratory of High Energies (VBLHE), Joint Institute for Nuclear Research Dubna Russia

¹⁷ University of Edinburgh United Kingdom

¹⁸ Friedrich Alexander Universität Erlangen-Nürnberg Germany

¹⁹ Northwestern University, Evanston U.S.A.

²⁰ Università di Ferrara and INFN Sezione di Ferrara, Ferrara Italy

²¹ Frankfurt Institute for Advanced Studies, Frankfurt Germany

²² Goethe Universität, Institut für Kernphysik, Frankfurt Germany

²³ INFN Laboratori Nazionali di Frascati Italy

²⁴ INFN Sezione di Genova Italy

²⁵ Justus Liebig-Universität Gießen II. Physikalisches Institut, Germany

²⁶ University of Glasgow United Kingdom

²⁷ Birla Institute of Technology and Science, Physics Department, Goa India

²⁸ Kernfysisch Versneller Instituut, University of Groningen Netherlands

²⁹ Gauhati University, Physics Department, Guwahati India

³⁰ Indian Institute of Technology Indore, School of Science, Indore India

³¹ Fachhochschule Südwestfalen Iserlohn Germany

^a e-mail: zambrana@kph.uni-mainz.de

- 32 Forschungszentrum Jülich, Institut für Kernphysik, Jülich Germany
 33 Chinese Academy of Science, Institute of Modern Physics, Lanzhou China
 34 INFN Laboratori Nazionali di Legnaro Italy
 35 Lunds Universitet, Department of Physics, Lund Sweden
 36 Johannes Gutenberg-Universität, Institut für Kernphysik, Mainz Germany
 37 Research Institute for Nuclear Problems, Belarus State University, Minsk Belarus
 38 Institute for Theoretical and Experimental Physics, Moscow Russia
 39 Moscow Power Engineering Institute, Moscow Russia
 40 Technische Universität München Germany
 41 Westfälische Wilhelms-Universität Münster Germany
 42 Indian Institute of Technology Bombay, Department of Physics, Mumbai India
 43 Nuclear Physics Division, Bhabha Atomic Research Centre, Mumbai India
 44 Suranaree University of Technology, Nakhon Ratchasima Thailand
 45 Budker Institute of Nuclear Physics of Russian Academy of Science, Novosibirsk Russia
 46 Novosibirsk State Technical University, Novosibirsk Russia
 47 Novosibirsk State University, Novosibirsk Russia
 48 Institut de Physique Nucléaire d'Orsay (UMR8608), CNRS/IN2P3 and Université Paris-sud, Orsay France
 49 Dipartimento di Fisica, Università di Pavia, INFN Sezione di Pavia, Pavia Italy
 50 Institute for High Energy Physics, Protvino Russia
 51 University of Sidney, School of Physics, Sidney Australia
 52 Kungliga Tekniska Högskolan, Stockholm Sweden
 53 Stockholms Universitet, Stockholm Sweden
 54 Petersburg Nuclear Physics Institute of Russian Academy of Science, Gatchina, St. Petersburg Russia
 55 Sardar Vallabhbhai National Institute of Technology, Applied Physics Department, Surat India
 56 Veer Narmand South Gujarat University, Department of Physics, Surat India
 57 Università di Torino and INFN Sezione di Torino, Torino Italy
 58 INFN Sezione di Torino, Torino Italy
 59 Politecnico di Torino and INFN Sezione di Torino, Torino Italy
 60 Università di Trieste and INFN Sezione di Trieste, Trieste Italy
 61 Universität Tübingen, Tübingen Germany
 62 The Svedberg Laboratory, Uppsala Sweden
 63 Uppsala Universitet, Institutionen för Strålningsvetenskap, Uppsala Sweden
 64 Universitat de Valencia Dpto. de Física Atómica, Molecular y Nuclear, Spain
 65 Sardar Patel University, Physics Department, Vallabh Vidynagar India
 66 National Centre for Nuclear Research, Warsaw Poland
 67 Österreichische Akademie der Wissenschaften, Stefan Meyer Institut für Subatomare Physik, Wien Austria
 68 IFPA, département AGO, Université de Liège, Liège Belgium

Received: date / Revised version: date

Abstract Baryon-to-meson Transition Distribution Amplitudes (TDAs) encoding valuable new information on hadron structure appear as building blocks in the collinear factorized description for several types of hard exclusive reactions. In this paper, we address the possibility of accessing nucleon-to-pion (πN) TDAs from $\bar{p}p \rightarrow e^+e^-\pi^0$ reaction with the future \bar{P} ANDA detector at the FAIR facility. At high center of mass energy and high invariant mass of the lepton pair q^2 , the amplitude of the signal channel $\bar{p}p \rightarrow e^+e^-\pi^0$ admits a QCD factorized description in terms of πN TDAs and nucleon Distribution Amplitudes (DAs) in the forward and backward kinematic regimes. Assuming the validity of this factorized description, we perform feasibility studies for measuring $\bar{p}p \rightarrow e^+e^-\pi^0$ with the \bar{P} ANDA detector. Detailed simulations on signal reconstruction efficiency as well as on rejection of the most severe background channel, *i.e.* $\bar{p}p \rightarrow \pi^+\pi^-\pi^0$ were performed for the center of mass energy squared $s = 5 \text{ GeV}^2$ and $s = 10 \text{ GeV}^2$, in the kinematic regions $3.0 < q^2 < 4.3 \text{ GeV}^2$ and $5 < q^2 < 9 \text{ GeV}^2$, respectively, with a neutral pion scattered in the forward or backward cone $|\cos\theta_{\pi^0}| > 0.5$ in the proton-antiproton center of mass frame. Results of the simulation show that the particle identification capabilities of the \bar{P} ANDA detector will allow to achieve a background rejection factor of $5 \cdot 10^7$ ($1 \cdot 10^7$) at low (high) q^2 for $s = 5 \text{ GeV}^2$, and of $1 \cdot 10^8$ ($6 \cdot 10^6$) at low (high) q^2 for $s = 10 \text{ GeV}^2$, while keeping the signal reconstruction efficiency at around 40%. At both energies, a clean lepton signal can be reconstructed with the expected statistics corresponding to 2 fb^{-1} of integrated luminosity. The future measurement of the signal channel cross section with \bar{P} ANDA will provide a new test of perturbative QCD description of a novel class of hard exclusive reactions and will open the possibility of experimentally accessing πN TDAs.

1 Introduction

Studies of hard exclusive reactions, such as Deeply Virtual Compton Scattering (DVCS) and Hard Exclusive Meson Electroproduction, within the collinear factorization approach, allow to challenge a QCD-based description of hadron structure (for a review see *e.g.* [1]). By separating the hard and soft stages of the interaction, at high energies the amplitudes of these reactions can be presented in form of convolutions of hard parts, computable in perturbation theory, and soft parts: generalized parton distributions (GPDs) and meson distribution amplitudes (DAs). These non-perturbative objects can be assigned a rigorous meaning in QCD and allow to interpret hadronic structural information in terms of quark and gluon degrees of freedom. Along with the usual parton distribution functions (PDFs) and form factors (FFs), GPDs encode valuable structural information about hadrons. In particular, GPDs are currently seen as a tool to study the nature and origin of the nucleon spin. Moreover, GPDs allow an extremely vivid interpretation in the impact parameter space as spatial femto-photographs of the hadron interior in the transverse plane.

Further development of the GPD approach led to the introduction of baryon-to-meson transition distribution amplitudes (TDAs) [2,3] broadening the class of hard reactions for which a factorized description of the scattering amplitudes for strong interaction phenomena can be applied. The physical picture encoded in baryon-to-meson TDAs is conceptually close to that contained in baryon GPDs and baryon DAs. Baryon-to-meson TDAs probe partonic correlations between states of different baryonic charge thus giving access to non-minimal Fock components of baryon light-cone wave functions. Fourier transforming TDAs to the impact parameter space allows one to perform femto-photography of hadrons from a new perspective. In particular, nucleon-to-pion (πN) TDAs may be used as a tool for spatial imaging of the structure of the pion cloud inside the nucleon. This opens a new window for the investigation of the various facets of the nucleon internal structure. A dedicated program for accessing πN TDAs in space-like regime through backward pion electroproduction [4,5] was proposed for J-Lab Hall B @ 11 GeV (see Ref. [6] for preliminary studies dedicated to J-Lab @ 6 GeV).

The future $\bar{\text{P}}\text{ANDA}$ (antiProton ANnihilations at DArmstadt) experiment at FAIR facility (Facility for Antiproton and Ion Research) operating a high-intensity antiproton beam with momentum up to 15 GeV offers unique possibilities for new investigations of the hadron structure (see Refs. [7,8]) complementing the results obtained from the studies of lepton beam induced reactions. In particular, the $\bar{\text{P}}\text{ANDA}$ experimental program includes dedicated measurements of the time-like electromagnetic form factors of the proton, mainly through the annihilation process $\bar{p}p \rightarrow e^+e^-$, for which feasibility studies with the $\bar{\text{P}}\text{ANDA}$ detector have already been performed at several antiproton beam energies [9]. The high intensity of the antiproton beam, together with the performance of the $\bar{\text{P}}\text{ANDA}$ detector, including particle identification capabilities, will render an unprecedented accuracy in the meas-

urements over a large range of four-momentum transferred squared, as shown by the simulations.

Outside the resonance region (*i.e.* for sufficiently high invariant mass of the lepton pair) the nucleon electromagnetic form factor admits a factorized description within the perturbative QCD approach [10,11]. This framework was further developed in [3,12] and was employed in [13,14] to provide a factorized description of nucleon-antinucleon annihilation into a highly virtual lepton pair and a pion in terms of πN TDAs and nucleon DAs. Note that a similar treatment can be applied to the scattering amplitude, when the lepton pair originates from a heavy charmonium state [15,16]. At lower energies, where factorization does not hold, descriptions of the $\bar{p}p \rightarrow e^+e^-\pi^0$ amplitude in terms of one-nucleon-exchanged model and the Regge theory [17,18] have been proposed, and preliminary studies of the cross section measurement with $\bar{\text{P}}\text{ANDA}$ have already been performed [19].

Thus, alongside with the time-like electromagnetic form factors measurements, it is extremely appealing to consider the possibility of accessing the proton/antiproton-pion TDAs with the $\bar{\text{P}}\text{ANDA}$ detector through the measurement of the differential cross section for the signal channel $\bar{p}p \rightarrow e^+e^-\pi^0$. In the present paper we address the feasibility of measuring the corresponding cross sections at high center of mass energy and high four-momentum transfer squared of the virtual photon, in the forward and backward angular regions, where the factorization theorem is expected to be valid [20]. Proton-antiproton annihilation in three pions, *i.e.* $\bar{p}p \rightarrow \pi^+\pi^-\pi^0$, appears as the most severe background channel for the previous process, as it contains the same number of particles in the final state, with identical charge signature. Detailed simulations have been performed on the signal reconstruction efficiency and on background rejection. The feasibility of the measurement using the statistics for an integrated luminosity of 2 fb^{-1} has also been studied.

2 Set-up of the future $\bar{\text{P}}\text{ANDA}$ experiment

An extensive description of the $\bar{\text{P}}\text{ANDA}$ detector can be found in Ref. [7]. Here we give a brief outline of the main components which are relevant to this analysis.

A High Energy Storage Ring (HESR), in which both stochastic and electron cooling systems are foreseen, will provide a high quality antiproton beam of momentum between 1.5 to 15 GeV. The conception of the detector, the read out and the data acquisition system is similar to that of other recently build detectors, such as ATLAS, CMS, COMPASS and BaBar. However, the high expected rate of $2 \cdot 10^7$ interactions per second and the multipurpose character of the detector, including the measurement of low cross sections in the charm sector, demand unique detection capabilities in $\bar{\text{P}}\text{ANDA}$. These include geometrical acceptance of almost 4π , energy and momentum resolutions at a few percent level, fast data acquisition and high radiation hardness. In the HESR high luminosity mode tuning, the average design luminosity of $\mathcal{L} = 1.5 \cdot 10^{32}$

$\text{cm}^{-2}\text{s}^{-1}$ will be reached with a pellet target of thickness $4 \cdot 10^{15}$ hydrogen atoms/ cm^2 , and 10^{11} stored antiprotons in HESR. The detector is divided in a target spectrometer area, in which the target is surrounded by a solenoid magnet providing up to 2 T magnetic field, and a forward spectrometer, based on a 2 Tm dipole magnet, to ensure particle detection at small polar angles, down to 2° . Tracking, particle identification, electromagnetic calorimetry and muon identification detectors are designed for both spectrometers. The reconstruction of the interaction point as well as secondary vertices is done with the microvertex detector (MVD). The concept of the MVD is based on radiation hard silicon pixel detectors with fast individual pixel readout circuits and silicon strip detectors, making a four layer barrel detector with an inner radius of 2.5 cm and an outer radius of 13 cm. The charged particle tracking and identification is provided by the straw tube tracker (STT), consisting of aluminized mylar tubes called “straws”, arranged in planar layers and mounted around the MVD in a total of 24 layers. Of these, the 8 central ones are tilted to achieve a resolution of 3 mm also in the direction parallel to the beam. Tracking detection at angles below 22° (not fully covered by the STT) is completed by three chambers of gas electron multiplier (GEM) detectors placed 1.1 m, 1.4 m and 1.9 m downstream the target. The chambers are designed to sustain a high counting rate of particles peaked at the most forward angles due to the relativistic boost of the reaction products. Additional components are required for the identification of hadrons and leptons in a wide kinematic range. For slow particles at large polar angles, particle identification will be provided by the time-of-flight (TOF) detector, with time resolution between 50 and 100 ps as required by the 50 – 100 cm of flight path in the target spectrometer. The PbWO_4 electromagnetic calorimeter (EMC), operated at -25°C , is designed for the detection of photons and electrons. Here, the fast scintillator material with short radiation length is required by the expected high counting rates and geometrically compact design of the target spectrometer. Crystals of 20 cm length, i.e. approximately 22 radiation lengths, are used in order to achieve an energy resolution below 2% at 1 GeV. For the efficient separation of pions from electrons at momenta $p < 1\text{ GeV}$, a barrel and a forward disk DIRC (detection of imaging reflected Cherenkov light) complete the PID system.

3 PANDA detector reconstruction capabilities

In the physics analysis, the generated events by the Monte Carlo programs (corresponding to signal or background channels) are, in a first step, passed through a full simulation of the PANDA detector, based on the GEANT 4 package [21], which takes care of the propagation of particles through the detector. Hit and energy loss information is then digitized according to a model simulating electronic properties, including electronic noise, yielding a response of the different detectors. The second step is the reconstruction of the relevant physical quantities for the identification of electrons, such as momentum, ratio of energy

loss to path length dE/dx in the STT, Cherenkov angle in the DIRC detectors, and energy deposit in the EMC from the simulated data. These two steps have been described in detail in Ref. [7], so we will give here only the main features which are relevant for the electron and photon identification.

The truncated arithmetic mean method is used on the dE/dx values for particle identification in order to exclude from the sample the largest values which correspond to the extended Landau tail of the distribution. The value used for the calculation of the arithmetic mean corresponds to the 70% out of the N individual dE/dx values. In this way a compromise between the requirements of the best resolution, defined through the width of a gaussian fit, and the smallest tail of the distribution is achieved. A resolution of $< 10\%$ in dE/dx is obtained for pions of momentum 1 GeV, which corresponds in average to four standard deviations of the distance between the truncated means for electrons and pions.

For the DIRC detector, the Cherenkov angle is given with a resolution $\sigma_C = \sigma_{C,\gamma}/\sqrt{N_{ph}}$, where the single photon resolution is $\sigma_{C,\gamma} = 10\text{ mrad}$. The number of detected photons, N_{ph} , has a dependence on the velocity and path length of the particle travelling inside the Cherenkov radiator. To calculate the Cherenkov angle, the software takes also into account the quantum efficiency of the photodetectors and the transmission and reflectivity losses in the detector material. A resolution of 2.3 mrad is obtained for pions of momentum 1 GeV [22]. The DIRC discrimination power is higher at lower energies due to the larger difference between the Cherenkov angles for pions and electrons: at momentum 500 MeV the difference in the angles for the Cherenkov light amounts to 36 mrad whereas at 1.5 GeV it is 4 mrad.

The most important detector for electron identification is the electromagnetic calorimeter. Electron identification is done using the ratio between the measured energy deposit and the reconstructed momentum E/p . In the electromagnetic calorimeter, the electrons deposit all (up to minor losses due to dead material, crystal edges, etc.) their energy via an electromagnetic shower, whereas muons and hadrons lose only a much lower fraction of their energy via Bethe-Bloch excitations and ionization processes. However, there could be cases in which a high energy deposit would be the consequence of hadronic interactions. In those cases the analysis of the shower shape plays an important role in the particle identification process. The Molière radius of PbWO_4 is 2 cm and it is of the order of the crystal front size dimensions, $2.1 \times 2.1\text{ cm}^2$ in the barrel and forward endcap and $2.44 \times 2.44\text{ cm}^2$ in the backward end cap of the calorimeter. In the case of an electromagnetic shower the largest fraction of the energy deposition is contained in a few crystals, whereas in the case of a hadronic interaction, the energy deposition will be distributed in a larger volume. The shower shape analysis uses the energy deposited in the central crystal of the cluster relative to that in the 3×3 or 5×5 crystal arrays surrounding it. The ratio between these two numbers is a measure for the cluster size and shape, and therefore it is

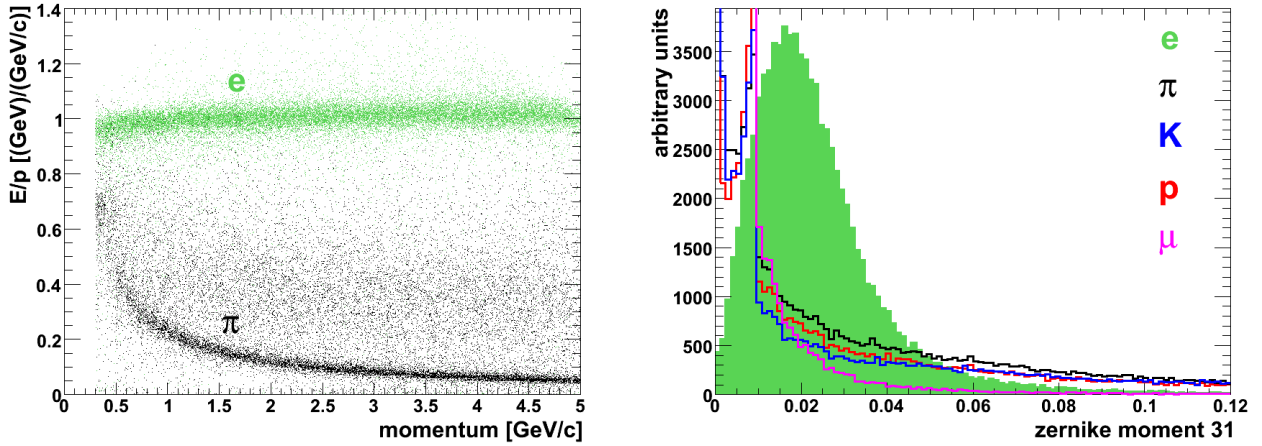


Figure 1. The ratio between the measured energy deposit and the reconstructed momentum E/p for an electron sample and for a pion sample (left) and the distribution of the Zernike moment 31 for samples of different particles species (right). The figures are taken from Ref. [7].

an indicator for an electromagnetic or a hadronic interaction. In addition, a set of four Zernike moments¹ are used to describe the spacial distribution of the energy within the shower by using polynomials in the radial and angular coordinates. Fig. 1 shows two examples on how E/p and one of the Zernike moments can be used to discriminate electrons from pions (for an extensive description, see Ref. [7], chapter 3, subsection 3.3.3).

Probabilities for the identification of a given particle using different hypothesis (electron, muon, pion, kaon and proton) are calculated on the basis of the results given by simulations using these species as input for the event generators for an extended range of momenta and polar angles. In addition to the variables discussed above, dE/dx information from the microvertex detector as well as hit information from the muon detector are included. In the case of the electromagnetic calorimeter, this probability is calculated using the output of a neural network which uses as the input the list of shower shape and Zernike parameters for a cluster described previously, as discussed in [7]. A global particle identification (PID) likelihood can be calculated using the individual subdetector likelihoods. Depending on the signal and background channels, the cuts for the particle identification can be adjusted to get the best signal efficiency for the required background suppression.

4 Theoretical overview and event generation

In this section we present a short overview of the basic definitions and conventions employed for the factorized

¹ The Zernike polynomials are a complete orthogonal set in the unit disk $0 < x^2 + y^2 < 1$. The projections of a function $f(x, y)$ on the basis of the Zernike polynomials are called the Zernike moments of f . Details can be found, for instance, in Ref. [23], chapter 9, section 2.

description of the nucleon-antinucleon annihilation into a high invariant mass lepton pair in association with a π^0 meson. The details can be found in Refs. [13, 14].

To the leading order in the electromagnetic coupling the reaction proceeds in two stages: firstly proton and anti-proton annihilate to produce a virtual photon and a neutral pion and subsequently the virtual photon decays into the lepton pair:

$$\begin{aligned} \bar{p}(p_1, s_1) + p(p_2, s_2) &\rightarrow \gamma^*(q) + \pi^0(k_3) \\ &\rightarrow e^+(k_1) + e^-(k_2) + \pi^0(k_3), \end{aligned} \quad (1)$$

where by $s_{1,2}$ we denote the antinucleon and nucleon spin variables.

According to the usual PANDA conventions, we choose the z axis along the colliding $\bar{p}p$ with the positive direction along the antinucleon beam. The two remaining spatial directions are referred to as the transverse plane. In order to specify the two kinematic regimes subject to the factorized description in terms of πN TDAs we switch to the light-cone variables and introduce the t - and u -channel light-cone vectors $n^t, p^t; n^u, p^u$ ($p^2 = n^2 = 0, 2p \cdot n = 1$). To quantify the longitudinal momentum transfers in the appropriate channels we define the t - and u -channel skewness variables

$$\xi^t \equiv -\frac{(k_3 - p_1) \cdot n^t}{(k_3 + p_1) \cdot n^t} \quad \xi^u \equiv -\frac{(k_3 - p_2) \cdot n^u}{(k_3 + p_2) \cdot n^u}. \quad (2)$$

The factorization mechanism suggested in [13] for the $\bar{p}(p_1) + p(p_2) \rightarrow \gamma^*(q) + \pi^0(k_3)$ subprocess of the reaction (1) is schematically depicted on Fig. 2. The amplitude is presented as a convolution of the hard part computed by means of perturbative QCD with nucleon DAs and nucleon-to-pion TDAs encoding the soft dynamics. The factorization is assumed to be achieved in two distinct kinematic regimes:

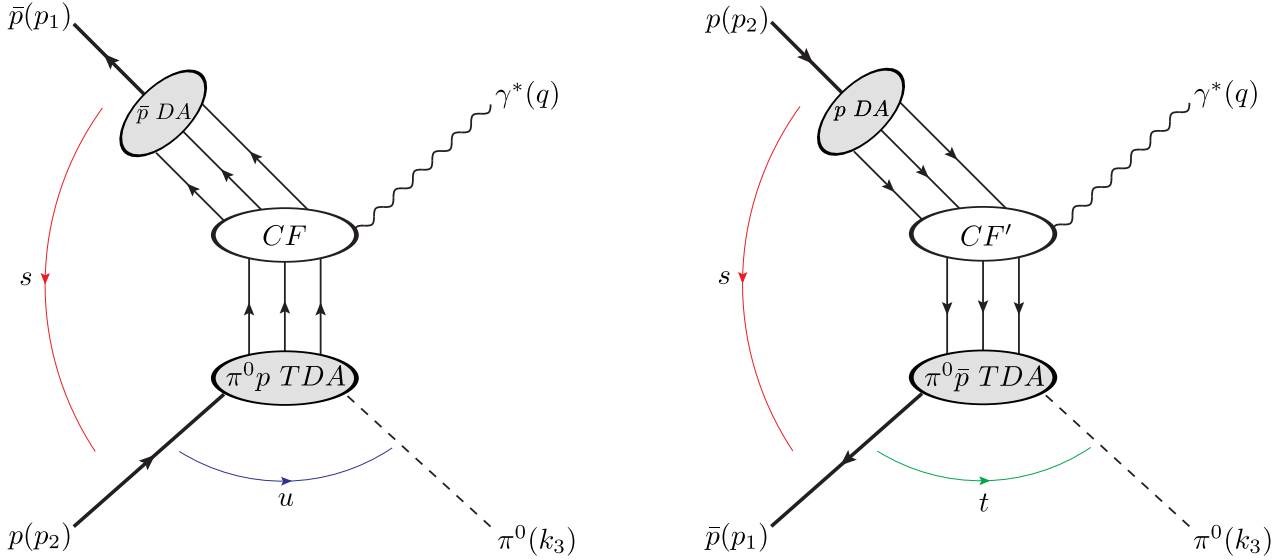


Figure 2. The two possibilities for factorization in the annihilation process $\bar{p}p \rightarrow \gamma^* \pi_0$, for both kinematics: backwards (left) and forward (right). \bar{p} (p) DA stands for the distribution amplitude of antiproton (proton). $\pi^0 p$ ($\pi^0 \bar{p}$) TDA stands for the transition distribution amplitude from a proton (antiproton) to a neutral pion. CF and CF' stand for coefficient functions (hard subprocess amplitudes).

- the near forward regime ($s = (p_1 + p_2)^2$, q^2 - large with ξ^t fixed; and $|t| = |(k_3 - p_1)^2| \sim 0$); it corresponds to the produced pion moving nearly in the direction of initial \bar{p} in $\bar{p}p$ center-of-mass (CM) system.
- the near backward regime ($s = (p_1 + p_2)^2$, q^2 - large with ξ^u fixed; and $|u| = |(k_3 - p_2)^2| \sim 0$); it corresponds to the produced pion moving nearly in the direction of initial p in $\bar{p}p$ CM.

The suggested reaction mechanism should manifest itself through the distinctive forward and backward peaks of the $\bar{p}p \rightarrow \gamma^* \pi^0$ cross section. The charge conjugation invariance results in the perfect symmetry between the two kinematic regimes. In what follows, for definiteness, we focus on the near forward kinematic regime. From now on we omit the labels referring to the particular (t - or u -) kinematic regime. However, all formulas for the near backward kinematics are essentially the same as in the forward kinematics (after interchanging the momenta). To the leading twist accuracy and to the leading order in the strong coupling α_s , the amplitude $\mathcal{M}_\lambda^{s_1 s_2}$ of $\bar{p}p \rightarrow \gamma^* \pi^0$ reads

$$\mathcal{M}_\lambda^{s_1 s_2} = \mathcal{C} \frac{1}{(q^2)^2} \left[S_\lambda^{s_1 s_2} \mathcal{I}(\xi, t) - S_\lambda'^{s_1 s_2} \mathcal{I}'(\xi, t) \right], \quad (3)$$

where

$$\mathcal{C} = -i \frac{(4\pi\alpha_s)^2 \sqrt{4\pi\alpha_{em}} f_N^2}{54 f_\pi}. \quad (4)$$

Here α_s and α_{em} are the strong and electromagnetic coupling constants, f_N stands for the nucleon wave function normalization constant, and $f_\pi = 93$ MeV denotes the pion weak decay constant. The spin structures in Eq. (3)

are defined as

$$\begin{aligned} S_\lambda^{s_1 s_2} &\equiv \bar{V}(p_1, s_1) \hat{\varepsilon}^*(\lambda) \gamma_5 U(p_2, s_2) \\ S_\lambda'^{s_1 s_2} &\equiv \frac{1}{M} \bar{V}(p_1, s_1) \hat{\varepsilon}^*(\lambda) \hat{\Delta}_T \gamma_5 U(p_2, s_2), \end{aligned} \quad (5)$$

where V and U are the usual nucleon Dirac spinors; $\Delta_T \equiv (k_3 - p_1)_T$ denotes the transverse t -channel momentum transfer and the Dirac “hat” notation $\hat{v} = \gamma_\mu v^\mu$ is employed. $\varepsilon(\lambda)$ stands for the polarization vector of the virtual photon. \mathcal{I} and \mathcal{I}' denote the convolution integrals of πN TDAs and nucleon DAs with the hard scattering kernels computed from the set of relevant scattering diagrams [4]. The averaged-squared amplitude for the process (1) then reads

$$\begin{aligned} |\overline{\mathcal{M}}_{\bar{p}p \rightarrow e^+ e^- \pi^0}|^2 &= \\ \frac{1}{4} \sum_{s_1, s_2, \lambda, \lambda'} \mathcal{M}_\lambda^{s_1 s_2} \frac{1}{q^2} e^2 \text{Tr} \left\{ \hat{k}_2 \hat{\varepsilon}(\lambda) \hat{k}_1 \hat{\varepsilon}^*(\lambda') \right\} \frac{1}{q^2} (\mathcal{M}_{\lambda'}^{s_1 s_2})^* . \end{aligned} \quad (6)$$

The differential cross section of the reaction (1) is expressed as

$$\frac{d\sigma}{dt dq^2 d\cos\theta_\ell^*} = \frac{\int d\varphi_\ell^* |\overline{\mathcal{M}}_{\bar{p}p \rightarrow e^+ e^- \pi^0}|^2}{64s(s - 4M^2)(2\pi)^4}, \quad (7)$$

where θ_ℓ^* and φ_ℓ^* are the lepton polar and azimuthal angles defined in e^+e^- center-of-mass frame (*i.e.* the γ^* rest frame).

To the leading twist accuracy, only the transverse polarization states of the virtual photon are contributing. Computing the relevant traces and integrating over the

lepton azimuthal angle one gets

$$\begin{aligned} & \int d\varphi_\ell^* |\overline{\mathcal{M}}^{\bar{p}p \rightarrow e^+e^-\pi^0}|^2 \Big|_{\text{Leading twist}} \\ &= 2\pi e^2 (1 + \cos^2 \theta_\ell^*) \frac{1}{4} |\mathcal{C}|^2 \frac{2(1+\xi)}{\xi(q^2)^4} \\ & \times (|\mathcal{I}(\xi, t)|^2 - \frac{\Delta_T^2}{M^2} |\mathcal{I}'(\xi, t)|^2) . \end{aligned} \quad (8)$$

Neglecting t and the nucleon mass squared M^2 with respect to large invariants s and q^2 (that is a reasonable approximation in the kinematic domain in which the factorized description is assumed to hold) the skewness parameter can be expressed as

$$\xi \simeq \frac{q^2}{2s - q^2} . \quad (9)$$

Thus, we work out the following expression for differential cross section of the reaction (1) within the factorized description in terms of πN TDAs in the near-forward kinematic regime:

$$\begin{aligned} & \frac{d\sigma}{dt dq^2 d\cos\theta_\ell^*} \Big|_{\text{Leading twist}} = \\ & \frac{K}{s - 4M^2} \frac{1}{(q^2)^5} (1 + \cos^2 \theta_\ell^*) , \end{aligned} \quad (10)$$

where

$$\begin{aligned} K &= \frac{(4\pi\alpha_{em})^2 (4\pi\alpha_s)^4 f_N^4}{64 \cdot 54^2 (2\pi)^3 f_\pi^2} \\ & \times (|\mathcal{I}(\xi, t)|^2 - \frac{\Delta_T^2}{M^2} |\mathcal{I}'(\xi, t)|^2) . \end{aligned} \quad (11)$$

The specific behaviour in $\cos^2 \theta_\ell^*$ of the cross section (10) together with the characteristic scaling behaviour in $1/q^2$ may be seen as a distinctive feature of the proposed factorization mechanism.

To compute the integral convolution $\mathcal{I}, \mathcal{I}'$ we use the revised version of the phenomenological model for πN TDAs suggested in Refs. [13,24]. Within this approach πN TDAs are constrained from the chiral dynamics and expressed through the nucleon DAs relying on the soft pion theorem. Certainly, this is an oversimplified πN TDA model that gives non-zero contribution only into the convolution \mathcal{I} . Moreover, within this model \mathcal{I} turns to be ξ - and t - independent. Nevertheless, this model is supposed to provide a reasonable estimate of the normalization for πN TDAs and can be taken as reliable at least for sufficiently small transverse momentum transfer. We refer the reader to [25] for the discussion on various phenomenological solutions for the nucleon DA and the relevant values of the strong coupling and nucleon wave function normalization constant. In the present analysis we use the Chernyak-Ogloblin-Zhitnitsky (COZ) [26] phenomenological solution for the nucleon DAs. This solution yields the value $|\mathcal{I}|^2 = 1.69 \cdot 10^9$, which is used in our evaluation. For the numerical estimates we use, following

Ref. [14], the mean value of the strong coupling $\alpha_s = 0.3$ and $f_N = 5.2 \cdot 10^{-3} \text{ GeV}^2$. The cross section (10) serves as the input for the event generator of the signal events $\bar{p}p \rightarrow e^+e^-\pi^0$ whose source code [27] was interfaced to the EvtGen [28] Monte Carlo.

For the cross section of the most severe background channel, i.e. three pion production $\bar{p}p \rightarrow \pi^+\pi^-\pi^0$, no theoretical calculations in the kinematic region of interest are available and the few low precision existing measurements [29,30,31,32,33] are not sufficient to constraint models. Inspired by the expectation for the total cross section ratio $\sigma(\bar{p}p \rightarrow \pi^+\pi^-)/\sigma(\bar{p}p \rightarrow e^+e^-) \sim 10^6$ (see [9,34] and references therein), we have assumed that the same relation holds for the case $\sigma(\bar{p}p \rightarrow \pi^+\pi^-\pi^0)/\sigma(\bar{p}p \rightarrow e^+e^-\pi^0)$. Even when data sets suggest that three pion production is about an order of magnitude higher than two pion production, the totally unknown $\bar{p}p \rightarrow e^+e^-\pi^0$ cross section supports the assumption on the signal to background ratio. In addition, we have assumed that the angular distributions for the three pion final state $\pi^+\pi^-\pi^0$ are identical to that of the signal final state $e^+e^-\pi^0$. With these considerations in mind, in the event generator for signal events, lepton masses and Monte Carlo identifiers were replaced by the ones corresponding to pions to account for background production. This conservative approach represents, from the experimental point of view, the most unfavored situation for background rejection. Having identical distributions for signal and background then requires to rely entirely on particle identification for the discrimination of signal and background events.

5 Event selection

Several simulations at the center of mass energy squared $s = 5 \text{ GeV}^2$ and $s = 10 \text{ GeV}^2$ were done using both simulated signal and background samples in order to determine signal reconstruction efficiency, background rejection power and feasibility of measuring the differential cross section for $\bar{p}p \rightarrow e^+e^-\pi^0$ with an integrated luminosity of 2 fb^{-1} .

The analysis procedure for the reconstruction of signal events was designed by tuning the selection cuts in a way that the signal to background ratio was kept to its maximum value in the kinematic region of the measurement. The reconstruction of $e^+e^-\pi^0$ candidates was done according to the following criteria:

- the event contains exactly two charged tracks of opposite sign;
- the particle associated to the negative track is identified by the PID software as an electron with minimum combined probability of 99% and, at least, with a minimum probability of 10% from each subdetector in PANDA;
- the particle associated to the positive track is identified by the PID software as a positron with minimum combined probability of 99% and, at least, with a minimum probability of 10% from each subdetector in PANDA;

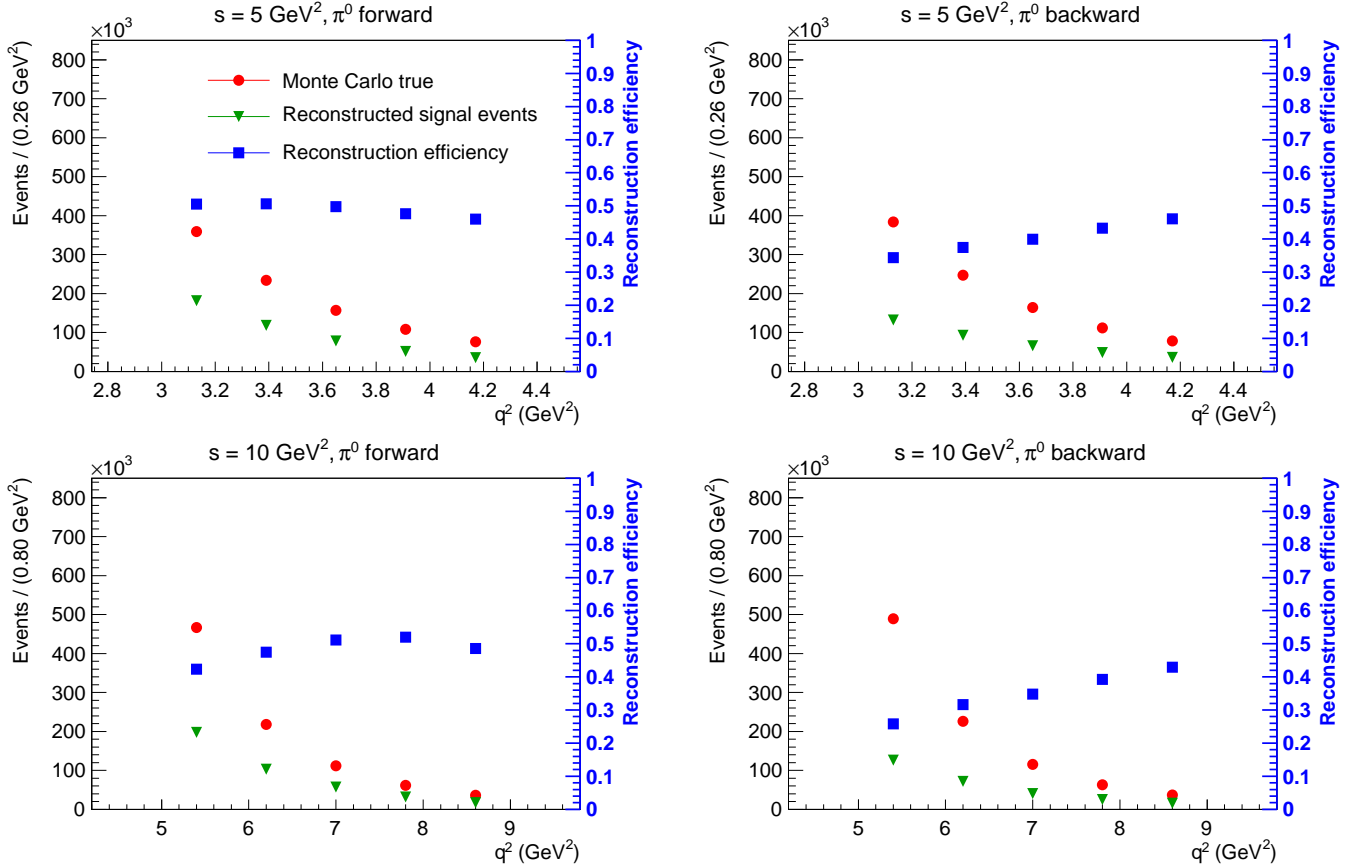


Figure 3. Monte Carlo true q^2 distribution for signal events (red dots), reconstructed signal events after event selection (green triangles) and signal reconstruction efficiency (blue squares) as a function of q^2 for $s = 5 \text{ GeV}^2$ and $s = 10 \text{ GeV}^2$, in both the t - (π^0 forward) and the u - (π^0 backward) channel kinematic regimes determined using independent statistical samples of 10^6 generated events.

- in the event, two photon candidates are reconstructed from two energy deposits in the EMC with a photon energy threshold $E_\gamma > 0.03 \text{ GeV}$ and no track associated, and combined to give a π^0 candidate with an invariant mass $0.115 < M(\gamma, \gamma) < 0.150 \text{ GeV}$.

At $s = 5 \text{ GeV}^2$ and $s = 10 \text{ GeV}^2$, signal events were measured in the kinematic range $3.0 < q^2 < 4.3 \text{ GeV}^2$ and $5 < q^2 < 9 \text{ GeV}^2$, respectively. In both cases, a π^0 candidate was reconstructed in the forward or backward region $|\cos \theta_{\pi^0}| > 0.5$, where the polar angle of the neutral pion is measured with respect to the direction of the antiproton in the $\bar{p}p$ center of mass system. The kinematic region of the measurement ensures that, at each $(q^2, \cos \theta_{\pi^0})$ point of the phase space, the appropriate cross channel momentum transfer squared (t or u for the forward and backward pion production, respectively) remains below 10% of the q^2 value, in order to preserve the applicability of the QCD collinear factorization description.

6 Signal reconstruction efficiency

High statistics simulations were done for the signal channel $\bar{p}p \rightarrow e^+e^-\pi^0$ in order to determine the efficiency

factors needed to correct raw data for detector effects, including efficiency in the reconstruction and bin migrations. On the basis of a full Monte Carlo simulation, the reconstruction efficiency measured in a given bin of a generic observable X is commonly defined as $\epsilon = N^R/N^G$, where N^R and N^G are the number of reconstructed and generated events found in that bin, with standard deviation $\Delta\epsilon = \sqrt{N^R}/N^G$ assuming a Poisson distribution. In our analysis, signal reconstruction efficiencies as a function of q^2 have been determined. Two full Monte Carlo simulations using 10^6 generated events each were performed at the center of mass energy squared $s = 5 \text{ GeV}^2$ in the q^2 range $3.0 < q^2 < 4.3 \text{ GeV}^2$, one in the t -channel regime, with the neutral pion in the forward region, and another one in the u -channel regime, with the neutral pion in the backward region. In an analogous way, two additional full simulations with the same statistics were performed at $s = 10 \text{ GeV}^2$, in the range $5 < q^2 < 9 \text{ GeV}^2$ also for both the t - and the u - channel regimes. The obtained reconstruction efficiencies in bins of q^2 are shown in Fig. 3 for all four cases. At $s = 5 \text{ GeV}^2$ the reconstruction efficiency shows a stable behaviour in q^2 , with an almost constant value around 50% in the t -channel regime, whereas in the

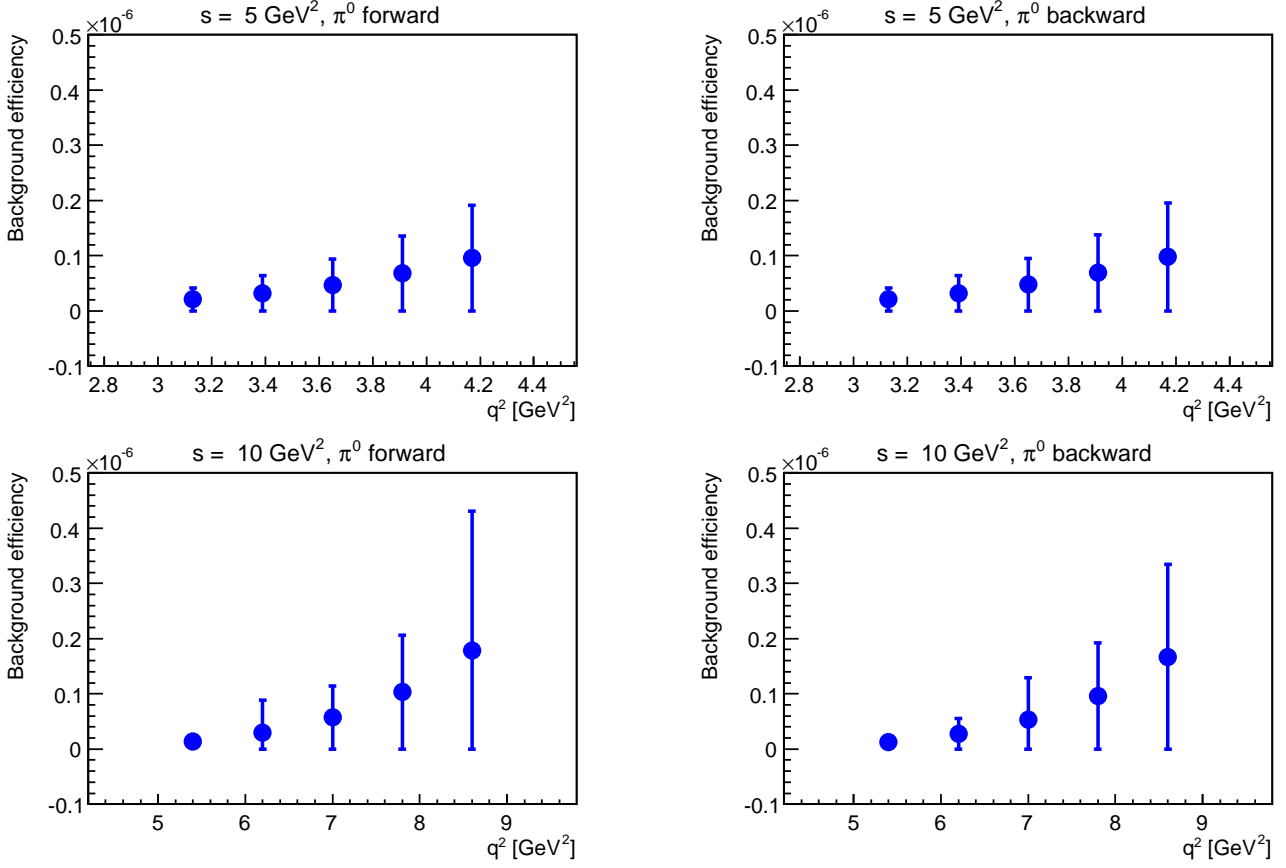


Figure 4. Upper limit for the background reconstruction efficiency at the confidence level of 67.3% as a function of q^2 for $s = 5 \text{ GeV}^2$ and $s = 10 \text{ GeV}^2$, in both the t - (π^0 forward) and the u - (π^0 backward) channel kinematic regimes determined using independent statistical samples of 10^8 generated events.

u -channel regime the efficiency exhibits an increasing pattern from 35% to 45% in the q^2 range. At $s = 10 \text{ GeV}^2$ a similar behaviour is observed, with a mean value of 45% in the t -channel regime and increasing the reconstruction efficiency from 25% to 45% with q^2 in the u -channel regime.

7 Background suppression

Analogous simulations to the ones described in Section 6 were performed using samples of 10^8 $\bar{p}p \rightarrow \pi^+\pi^-\pi^0$ generated events in order to measure the background suppression power achieved by the selection criteria defined in Section 5. At $s = 5 \text{ GeV}^2$ and for both the t - and the u -channel regimes, no pions were found after event selection. At $s = 10 \text{ GeV}^2$, four $\pi^+\pi^-\pi^0$ events were misidentified as $e^+e^-\pi^0$ events in the t -channel regime, whereas in the u -channel regime only one background event survived the cuts. The background suppression factor is defined as the inverse of the probability that a $\pi^+\pi^-\pi^0$ event is misidentified as a $e^+e^-\pi^0$ event. This probability can in fact be measured as the “efficiency” in the reconstruction of background events when a $\pi^+\pi^-\pi^0$ sample is filtered by an algorithm designed to reconstruct $e^+e^-\pi^0$ events. For

this reason, we denote this probability as ϵ_B . In situations of high suppression like this one, where only a few or even no events are reconstructed in a given bin, the standard estimation of efficiency and its error based on binomial or Poisson distributions gives results in contradiction with intuition. For instance, if no pion event is reconstructed in a given bin, the value for the efficiency would be zero with complete certainty (zero error) according to the Poisson distribution. We can still in this case estimate an *upper limit* for ϵ_B at some value of confidence level, depending on the available statistics. In this analysis, to measure the reconstruction efficiency and its error, a Bayesian approach which exhibits reasonable behaviour in the limit of high suppression has been used to treat the background channel (see Ref. [35] for a review). At the 67.3% of confidence level (i.e. one sigma) estimators of the upper limit of ϵ_B and its standard deviation $\Delta\epsilon_B$ are given by the relations [35]:

$$\epsilon_B = \frac{N^R + 1}{N^G + 2}$$

$$\Delta\epsilon_B = \sqrt{\left(\frac{N^R + 1}{N^G + 2}\right) \left\{ \frac{N^R + 2}{N^G + 3} - \frac{N^R + 1}{N^G + 2} \right\}}. \quad (12)$$

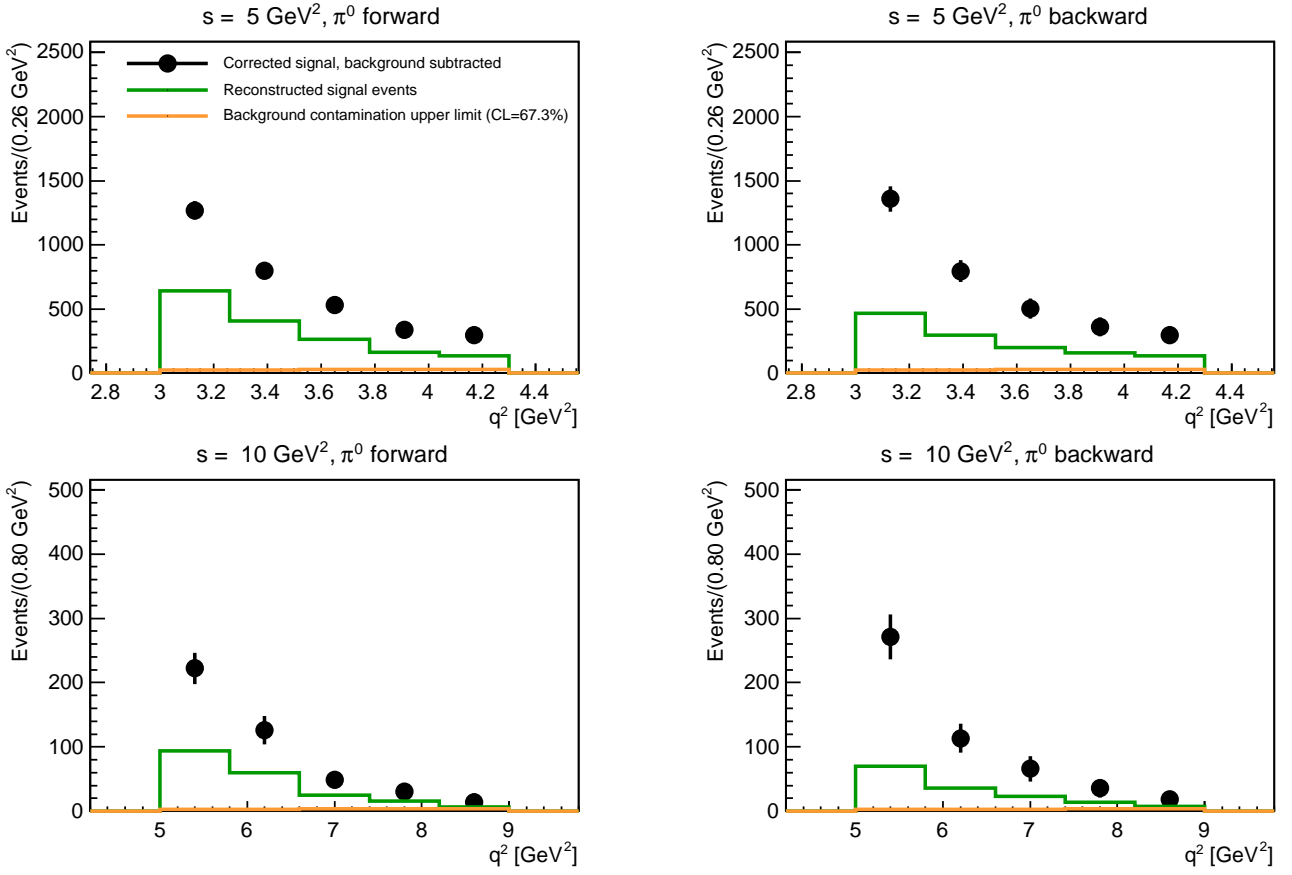


Figure 5. The reconstructed signal after event selection (green), the expected upper limit background contamination at the 67.3% of confidence level (orange) and the reconstructed, efficiency-corrected signal after background subtraction (black) in bins of q^2 , for $s = 5 \text{ GeV}^2$ and $s = 10 \text{ GeV}^2$ in both the t - (π^0 forward) and the u - (π^0 backward) channel kinematic regimes using statistical samples of integrated luminosity $\mathcal{L} = 2 \text{ fb}^{-1}$.

For the two energies simulated and in both, the t - and the u -channel regimes, misidentification probabilities in bins of q^2 have been estimated in this way and are displayed in Fig. 4. The inverse $1/\epsilon_B$ then yields the suppression factor. At $s = 5 \text{ GeV}^2$, the simulations show that the background suppression factor goes from $5 \cdot 10^7$ at low q^2 down to $1 \cdot 10^7$ at large q^2 . At $s = 10 \text{ GeV}^2$, the background suppression factor goes from $1 \cdot 10^8$ at low q^2 down to $6 \cdot 10^6$ at large q^2 . Under the assumption of a background to signal cross section ratio $\sigma(\bar{p}p \rightarrow \pi^+\pi^-\pi^0)/\sigma(\bar{p}p \rightarrow e^+e^-\pi^0) = 10^6$, this means that the background pollution in a signal sample will remain at the level of a few percent after event selection for low q^2 , whereas at larger values of q^2 it can be kept below 20%. In case the cross section ratio is much larger than 10^6 , a better background suppression can be achieved at the cost of reducing the signal efficiency. The estimated upper limit of background pollution in a signal sample, necessary for the subsequent statistical subtraction, is discussed in detail in Appendix B.

8 Feasibility of measuring the $\bar{p}p \rightarrow e^+e^-\pi^0$ differential cross section using an integrated luminosity $\mathcal{L} = 2 \text{ fb}^{-1}$

The feasibility of measuring the production cross section for the signal channel $\bar{p}p \rightarrow e^+e^-\pi^0$ requires simulations using the expected statistics corresponding to some particular value of integrated luminosity. Running periods with the average design luminosity of $1.5 \cdot 10^{32} \text{ cm}^{-2} \text{ s}^{-1}$ will provide 2 fb^{-1} of integrated luminosity in PANDA [7]. In order to estimate the corresponding statistics, we have first extrapolated the differential cross section given by Eq. (10), which corresponds to the limit of neutral pion with zero transverse momentum, into the forward and backward cone $|\cos\theta_{\pi_0}| > 0.5$. Second, the extrapolated differential cross section was integrated in the kinematic region of the measurement. At $s = 5 \text{ GeV}^2$, integration in the range $3.0 < q^2 < 4.3 \text{ GeV}^2$ and $|\cos\theta_{\pi_0}| > 0.5$ gave a value of 1675 fb for the integrated cross section. At $s = 10 \text{ GeV}^2$, integration in the range $5 < q^2 < 9 \text{ GeV}^2$ and $|\cos\theta_{\pi_0}| > 0.5$ gave a value of 233 fb for the integrated cross section. Details on the extrapolation and integration of the differential cross section in a two di-

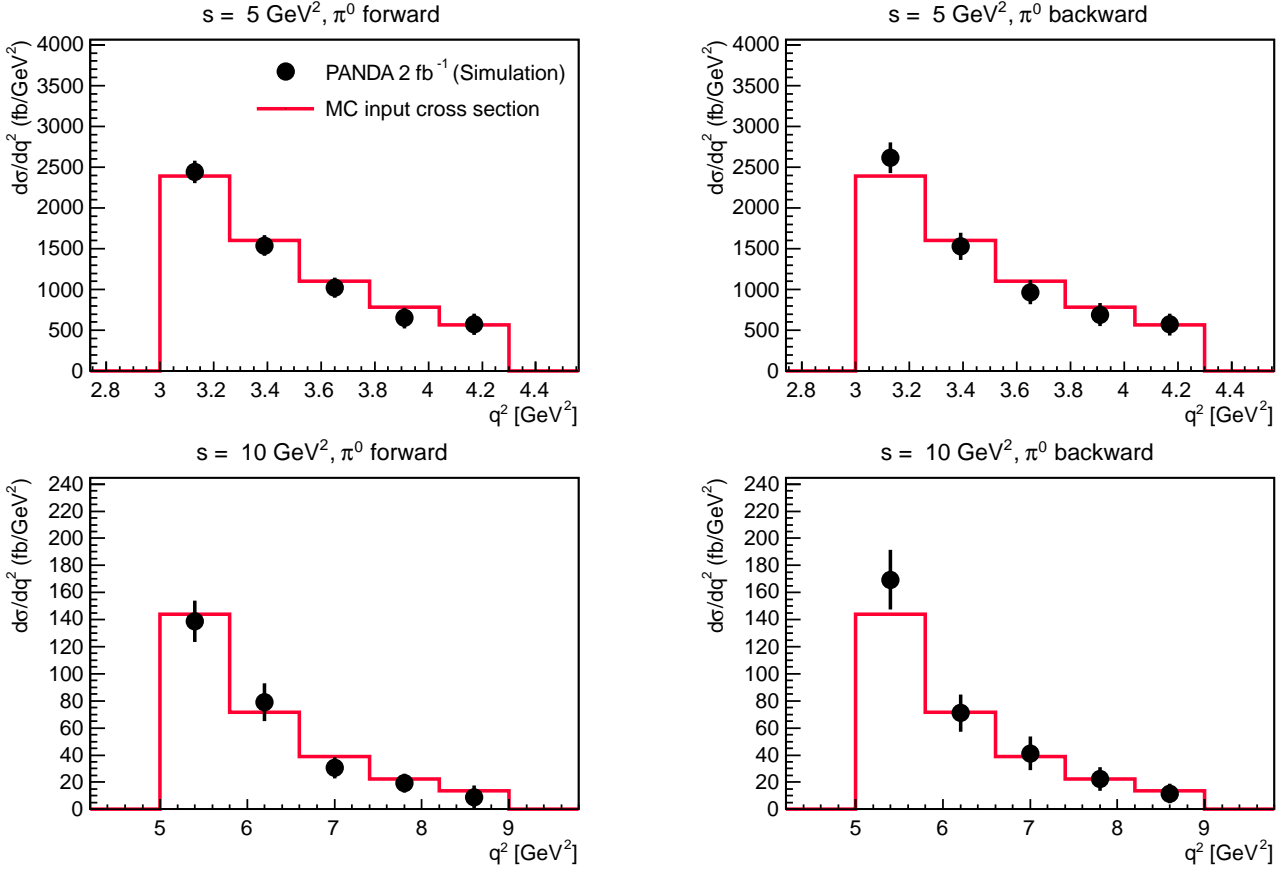


Figure 6. The “measured” (background subtracted) $\bar{p}p \rightarrow e^+e^-\pi^0$ differential cross section with the simulation $(d\sigma/dq^2)_{\text{meas}}$ in bins of q^2 with a statistical sample of integrated luminosity $\mathcal{L} = 2 \text{ fb}^{-1}$, compared to the theoretical input in the Monte Carlo, for $s = 5 \text{ GeV}^2$ and $s = 10 \text{ GeV}^2$, in both the t - (π^0 forward) and the u - (π^0 backward) channel kinematic regimes.

mensional bin ($\Delta q^2, \Delta \cos \theta_{\pi_0}$) can be found in Appendix A. The expected number of signal events in PANDA using $\mathcal{L} = 2 \text{ fb}^{-1}$ are then 3350 and 465 at $s = 5 \text{ GeV}^2$ and $s = 10 \text{ GeV}^2$, respectively, both in the t - and the u -channel kinematic regimes. For each value of s , two full simulations have been performed using these statistical samples in both channels. Then, the raw reconstructed distributions have been corrected bin by bin in q^2 with the efficiency factors ϵ determined by the high statistics simulations described in Section 6. In addition, in each of the simulations and for each q^2 bin, the remaining background contamination which would survive the selection of signal events in a data sample of 2 fb^{-1} has been estimated. The estimation was done on the basis of the background efficiency factors discussed in Section 7 (Eq. (12)) and assuming a ratio $\sigma(\bar{p}p \rightarrow \pi^+\pi^-\pi^0)/\sigma(\bar{p}p \rightarrow e^+e^-\pi^0) = 10^6$. Consequently, the statistical error in the number of reconstructed signal events N^R has been corrected to take into account the subtraction of the estimated upper limit background contamination. Details on the background subtraction procedure are given in Appendix B. An upper limit of background pollution at the level of a few percent is expected at low q^2 , remaining below 20% at large values of q^2 . The raw reconstructed signal after event selection,

the expected upper limit background contamination, and the efficiency-corrected signal after background subtraction are shown in Fig. 5 for the two energies simulated, in both the t - and the u -channel regimes. The “measured” differential cross section obtained from the simulation in a q^2 bin with width Δq^2 (integrated over $\cos \theta_{\pi_0} > 0.5$ in the t -channel regime and over $\cos \theta_{\pi_0} < -0.5$ in the u -channel regime), is then determined as:

$$\left(\frac{d\sigma}{dq^2}\right)_{\text{meas}} = \frac{N^R}{\epsilon \cdot \mathcal{L} \cdot \Delta q^2}. \quad (13)$$

The simulated “measured” differential cross section in bins of q^2 together with the input cross section in the Monte Carlo $(d\sigma/dq^2)_{\text{MC}}$ are shown in Tables 1 and 2 and are displayed in Fig. 6. For the comparison, the input cross section in the Monte Carlo, which follows a $1/(q^2)^5$ distribution (see Eq. (10)), was normalized to the value of the integrated cross section in the kinematic region of the measurement. At $s = 5 \text{ GeV}^2$, the expected precision of the measurement goes from 6% at low q^2 to 23% at high q^2 in both the t - and u -channel regime. At $s = 10 \text{ GeV}^2$, the statistical error goes from 11% up to 90% in the t -channel regime, and from 10% up to 60% in the u -channel regime. The results show that the signal channel identification and

Table 1. The “measured” differential cross section obtained with the simulations $(d\sigma/dq^2)_{\text{meas}}$ and its statistical error Δ_{stat} in bins of q^2 , compared to the input cross section in the Monte Carlo $(d\sigma/dq^2)_{\text{MC}}$, for $s = 5 \text{ GeV}^2$ in both the t - and the u -channel kinematic regimes. In each q^2 bin, the cross section is integrated in $|\cos\theta_{\pi^0}| > 0.5$.

$s = 5 \text{ GeV}^2$, t -channel (π^0 forward)			
q^2 bin (GeV ²)	$(d\sigma/dq^2)_{\text{meas}}$ (fb/GeV ²)	Δ_{stat} (fb/GeV ²)	$(d\sigma/dq^2)_{\text{MC}}$ (fb/GeV ²)
3.00, 3.26	2441	139	2388
3.26, 3.52	1538	128	1600
3.52, 3.78	1024	124	1105
3.78, 4.04	650	125	782
4.04, 4.30	573	130	567

$s = 5 \text{ GeV}^2$, u -channel (π^0 backward)			
q^2 bin (GeV ²)	$(d\sigma/dq^2)_{\text{meas}}$ (fb/GeV ²)	Δ_{stat} (fb/GeV ²)	$(d\sigma/dq^2)_{\text{MC}}$ (fb/GeV ²)
3.00, 3.26	2615	190	2388
3.26, 3.52	1529	165	1600
3.52, 3.78	969	150	1105
3.78, 4.04	693	138	782
4.04, 4.30	572	132	567

Table 2. The “measured” differential cross section obtained with the simulations $(d\sigma/dq^2)_{\text{meas}}$ and its statistical error Δ_{stat} in bins of q^2 , compared to the input cross section in the Monte Carlo $(d\sigma/dq^2)_{\text{MC}}$, for $s = 10 \text{ GeV}^2$ in both the t - and the u -channel kinematic regimes. In each q^2 bin, the cross section is integrated in $|\cos\theta_{\pi^0}| > 0.5$.

$s = 10 \text{ GeV}^2$, t -channel (π^0 forward)			
q^2 bin (GeV ²)	$(d\sigma/dq^2)_{\text{meas}}$ (fb/GeV ²)	Δ_{stat} (fb/GeV ²)	$(d\sigma/dq^2)_{\text{MC}}$ (fb/GeV ²)
5.0, 5.8	139	15	144
5.8, 6.6	79	14	72
6.6, 7.4	31	8	39
7.4, 8.2	19	7	23
8.2, 9.0	9	8	14

$s = 10 \text{ GeV}^2$, u -channel (π^0 backward)			
q^2 bin (GeV ²)	$(d\sigma/dq^2)_{\text{meas}}$ (fb/GeV ²)	Δ_{stat} (fb/GeV ²)	$(d\sigma/dq^2)_{\text{MC}}$ (fb/GeV ²)
5.0, 5.8	169	22	144
5.8, 6.6	71	14	72
6.6, 7.4	41	12	39
7.4, 8.2	22	9	23
8.2, 9.0	12	7	14

background separation at $s = 5 \text{ GeV}^2$ is feasible, with averaged statistical precision of 12% (excluding the last q^2 bin with poor statistics). At $s = 10 \text{ GeV}^2$, the lower statistics increases the averaged uncertainty to 25%.

9 Conclusions and outlook

In the framework of the $\bar{\text{P}}\text{ANDA@FAIR}$ experiment, cross section measurements of nucleon-antinucleon annihilation into a highly virtual lepton pair in association with a pion emitted in the forward or the backward region will represent a novel test of the QCD collinear factorization approach of hard exclusive reactions providing experimental access to the πN TDAs.

In this paper we addressed the feasibility of measuring $\bar{p}p \rightarrow e^+e^-\pi^0$ with the $\bar{\text{P}}\text{ANDA}$ detector for the center of mass energy squared $s = 5 \text{ GeV}^2$ and $s = 10 \text{ GeV}^2$ for the kinematic regimes in which the factorized description of the process in terms of πN TDAs and proton DAs can be assumed. For $s = 5 \text{ GeV}^2$, the kinematic region of the measurement was $3.0 < q^2 < 4.3 \text{ GeV}^2$, with the neutral pion scattered into the forward (or backward) cone selected by the condition $|\cos\theta_{\pi^0}| > 0.5$. For $s = 10 \text{ GeV}^2$, the kinematic region of the measurement was $5 < q^2 < 9 \text{ GeV}^2$, with $|\cos\theta_{\pi^0}| > 0.5$.

The input cross section for the event generator of signal events is a leading twist, leading order calculation which uses πN TDAs and nucleon DAs within the collinear factorization approach. In our studies we employed the simple πN TDA model constraining πN TDAs from chiral dynamics in terms of nucleon DAs. This model is argued to provide a reliable normalization for πN TDAs for the pion being produced exactly in the forward (backward) direction. Therefore, this model at least represents a reasonable first step approximation. Future detailed feasibility studies will require the use of a more sophisticated phenomenological model proposed for πN TDAs in [5] based on the spectral representation for baryon-to-meson TDAs in terms of quadruple distributions [36]. Another possibility is given by the calculations of πN TDAs within the light-cone quark model approach [37].

Our simulations at $s = 5 \text{ GeV}^2$ show that $\bar{\text{P}}\text{ANDA}$ particle identification capabilities will allow a suppression of the hadronic background $\bar{p}p \rightarrow \pi^+\pi^-\pi^0$ at the level of $5 \cdot 10^7$ at low q^2 , decreasing to $1 \cdot 10^7$ for the larger values of q^2 . At $s = 10 \text{ GeV}^2$, the suppression factor remains around $1 \cdot 10^8$ at low q^2 , down to $6 \cdot 10^6$ for large q^2 . For both energies, the signal reconstruction efficiency is kept of the order of 40% on average. We expect, in consequence, that the pion pollution in the signal sample will remain at the level of a few percent at low q^2 , and under control below 20% for larger values of four-momentum transfer squared. The dedicated studies we performed using the expected statistics corresponding to the integrated luminosity of 2 fb^{-1} show that the future measurement of the production differential cross section in bins of q^2 is feasible with $\bar{\text{P}}\text{ANDA}$, with averaged statistical uncertainty of 12% at $s = 5 \text{ GeV}^2$, and with averaged statistical uncertainty of

25% at $s = 10 \text{ GeV}^2$. These results are promising concerning the experimental perspectives for accessing πN TDAs with PANDA. Other kinematic regions and other processes [15, 38] related to TDAs should be scrutinized in a similar way to evaluate their feasibility.

This work has been supported by the Carl-Zeiss-Stiftung under grant number 21-0563-2.8/122/1 and 21-0563-2.8/131/1 and by the Bundesministerium für Bildung und Forschung (BMBF), under grant number 05P12UMFP9. We would like to thank B. Pire, L. Szymanowski and J.P. Lansberg for constructive and stimulating discussions, lots of explanations on the topic of the TDAs and for a careful reading of the manuscript. Finally, we are very grateful to D. Djukanovic for his invaluable work in maintaining the dedicated HIMSTER cluster at Helmholtz-Institut Mainz, where all our simulations have been performed.

A Integration in a $(\Delta q^2, \Delta \cos \theta_{\pi^0})$ bin

In this appendix we describe the extrapolation and integration of the differential cross section (10) in the kinematic region of the measurement defined by the two dimensional bin $(\Delta q^2, \Delta \cos \theta_{\pi^0})$.

The kinematics of $\bar{p}(p_1)p(p_2) \rightarrow \gamma^*(q)\pi^0(k_3)$ is most easily solved in the CM frame, where the total three momentum of both the initial and final state is zero. By convention, the direction of the antiproton defines the positive direction z of the coordinate system. Also by convention, the x axis of the coordinate system is chosen to be perpendicular to the scattering plane. With this choice, the four momenta of the initial and final state particles become

$$\begin{aligned} p_1 &= (E, 0, 0, k_i) \\ p_2 &= (E, 0, 0, -k_i) \\ q &= (E_\gamma, 0, -k_f \sin \theta_{\pi^0}, -k_f \cos \theta_{\pi^0}) \\ k_3 &= (E_{\pi^0}, 0, k_f \sin \theta_{\pi^0}, k_f \cos \theta_{\pi^0}), \end{aligned} \quad (14)$$

with energies given by $E = \sqrt{M^2 + k_i^2}$, $E_\gamma = \sqrt{q^2 + k_f^2}$ and $E_{\pi^0} = \sqrt{m_{\pi^0}^2 + k_f^2}$. The condition $2E = \sqrt{s}$ fixes the three momentum modulus squared of both proton and antiproton to be

$$k_i^2 = \frac{1}{4}(s - 4M^2). \quad (15)$$

In the same way, the energy conservation relation in the final state $E_\gamma + E_{\pi^0} = \sqrt{s}$ fixes the momentum of virtual photon and neutral pion, with the result

$$k_f^2 = \frac{1}{4s} [s^2 - 2(q^2 + m_{\pi^0}^2)s + (q^2 - m_{\pi^0}^2)^2]. \quad (16)$$

Using the four momenta given by Eq. (14), the antiproton to pion four momentum transfer squared $t \equiv (p_1 - k_3)^2$ is given by

$$\begin{aligned} t &= (p_1 - k_3)^2 \\ &= p_1^2 + k_3^2 - 2p_1 \cdot k_3 \\ &= M^2 + m_{\pi^0}^2 - 2(E E_{\pi^0} - k_i k_f \cos \theta_{\pi^0}), \end{aligned} \quad (17)$$

which can be written as

$$t = \frac{1}{2} [m_{\pi^0}^2 + \cos \theta_{\pi^0} \sqrt{1 - 4M^2/s} \Lambda(s, q^2, m_{\pi^0}^2) + 2M^2 + q^2 - s], \quad (18)$$

with $\Lambda(x, y, z) \equiv \sqrt{x^2 + y^2 + z^2 - 2xy - 2xz - 2yz}$. Eq. (18) expresses the dependence of the variable t on q^2 and $\cos \theta_{\pi^0}$ for a given value of the center of mass energy squared s .

The integration of the leptonic phase space degrees of freedom in Eq. (10) is straightforward:

$$\begin{aligned} \frac{d\sigma}{dt dq^2} \Big|_{\Delta_T=0} &= \int_{-1}^1 d \cos \theta_\ell^* \frac{d\sigma}{dt dq^2 d \cos \theta_\ell^*} \Big|_{\Delta_T=0} \\ &= \frac{8}{3} K \frac{1}{s - 4M^2} \frac{1}{(q^2)^5}. \end{aligned} \quad (19)$$

The integration of this equation in the two dimensional bin $(\Delta q^2, \Delta \cos \theta_{\pi^0})$ defined by the limits $q_1^2 < q^2 < q_2^2$ and $\cos \theta_1 < \cos \theta_{\pi^0} < 1$ is done by first mapping the $\cos \theta$ boundaries to the (q^2 dependent) t boundaries as given by Eq. (18): $\cos \theta_1 < \cos \theta < 1 \Rightarrow t_{\text{cut}}(q^2) < t < t_{\text{max}}(q^2)$, with $t_{\text{cut}}(q^2) \equiv t(\cos \theta_1, q^2)$ and $t_{\text{max}}(q^2) \equiv t(1, q^2)$. Extrapolating the differential cross section (19) (obtained at $\cos \theta_{\pi^0} = 1$) to the angular region $\cos \theta_1 < \cos \theta_{\pi^0} < 1$, the integration in the two dimensional bin $(\Delta q^2, \Delta \cos \theta_{\pi^0})$ is done as

$$\begin{aligned} \sigma &= \int_{q_1^2}^{q_2^2} dq^2 \int_{t_{\text{cut}}(q^2)}^{t_{\text{max}}(q^2)} dt \frac{d\sigma}{dq^2 dt} \Big|_{\Delta_T=0} \\ &= \frac{8}{3} K \frac{1}{s - 4M^2} \int_{q_1^2}^{q_2^2} dq^2 \frac{1}{(q^2)^5} [t_{\text{max}}(q^2) - t_{\text{cut}}(q^2)]. \end{aligned} \quad (20)$$

For the estimates used in this analysis, the q^2 integration in Eq. (20) has been done numerically.

B Background subtraction

In this appendix we describe the background subtraction procedure carried out in our analysis. For the clarity of the notation, we will refer to the signal channel $\bar{p}p \rightarrow e^+e^-\pi^0$ with the subscript S , and we will refer to the background channel $\bar{p}p \rightarrow \pi^+\pi^-\pi^0$ with the subscript B . In a data sample with luminosity \mathcal{L} , the expected number of signal and background events produced in an experiment is $N_S = \sigma_S \mathcal{L}$ and $N_B = \sigma_B \mathcal{L}$. After the event selection procedure, the expected number of reconstructed signal and background events becomes $N_S^R = \epsilon_S \sigma_S \mathcal{L}$ and $N_B^R = \epsilon_B \sigma_B \mathcal{L}$, where ϵ_S and ϵ_B are the reconstruction efficiencies for the signal and background channels. We remark that due to the high background suppression, ϵ_B is

understood as an upper limit for the background reconstruction efficiency estimated at some confidence level, as discussed in Section 7. In consequence, N_B^R is also understood as an upper limit for background contamination, estimated at the same confidence level. The total number of observed events in the sample used for the measurement is therefore $N^R = N_S^R + N_B^R$, for which we assume a Poisson distribution with standard deviation $\Delta N^R = \sqrt{N^R}$. The estimation of the number of signal events in this sample is then done by subtracting the remaining background contamination, and assuming standard error propagation:

$$N_S^R = N^R - N_B^R, \quad (\Delta N_S^R)^2 = (\Delta N^R)^2 + (\Delta N_B^R)^2. \quad (21)$$

The estimation of the background contamination $N_B^R = \epsilon_B \sigma_B \mathcal{L}$ requires the knowledge of the cross section σ_B , which can be measured with PANDA. In our analysis, however, we simply assume the relation $\sigma_B = 10^6 \sigma_S$. The computation of the standard deviation is also determined by simple error propagation, according to

$$\left(\frac{\Delta N_B^R}{N_B^R} \right)^2 = \left(\frac{\Delta \epsilon_B}{\epsilon_B} \right)^2 + \left(\frac{\Delta \sigma_B}{\sigma_B} \right)^2. \quad (22)$$

Relying on the fact that the cross section corresponding to three pion production from $\bar{p}p$ annihilation will be measured at PANDA with great precision due to its high statistics, we have neglected the last term $\Delta \sigma_B / \sigma_B$ in our analysis.

References

1. S. Boffi and B. Pasquini, Riv. Nuovo Cim. **30**, 387 (2007).
2. L. L. Frankfurt, P. V. Pobylitsa, M. V. Polyakov and M. Strikman, Phys. Rev. D **60**, 014010 (1999).
3. B. Pire and L. Szymanowski, Phys. Rev. D **71**, 111501 (2005).
4. J. P. Lansberg, B. Pire and L. Szymanowski, Phys. Rev. D **75**, 074004 (2007) [Erratum-ibid. D **77**, 019902 (2008)].
5. J. P. Lansberg, B. Pire, K. Semenov-Tian-Shansky and L. Szymanowski, Phys. Rev. D **85**, 054021 (2012).
6. A. Kubarovskiy, AIP Conf. Proc. **1560**, 576 (2013).
7. M. F. M. Lutz *et al.* [PANDA Collaboration], “Physics Performance Report for PANDA: Strong Interaction Studies with Antiprotons” arXiv:0903.3905 [hep-ex].
8. U. Wiedner, Prog. Part. Nucl. Phys. **66**, 477-518 (2011).
9. M. Sudol, M. C. Mora Espí *et al.*, Eur. Phys. J. A **44**, 373 (2010).
10. G. P. Lepage, S. J. Brodsky, Phys. Rev. D **22**, 2157 (1980).
11. V. L. Chernyak and A. R. Zhitnitsky Phys. Rept. **112**, 173 (1984).
12. B. Pire and L. Szymanowski, Phys. Lett. B **622** 83 (2005).
13. J. P. Lansberg, B. Pire and L. Szymanowski, Phys. Rev. D **76**, 111502 (2007).
14. J. P. Lansberg, B. Pire, K. Semenov-Tian-Shansky and L. Szymanowski, Phys. Rev. D **86**, 114033 (2012).
15. B. Pire, K. Semenov-Tian-Shansky and L. Szymanowski, Phys. Lett. B **724**, 99 (2013).
16. B. Ma, B. Pire, K. Semenov-Tian-Shansky and L. Szymanowski, arXiv:1402.0413 [hep-ph].
17. C. Adamuscin, E. A. Kuraev, E. Tomasi-Gustafsson and F. E. Maas, Phys. Rev. C **75**, 045205 (2007).
18. J. Guttman and M. Vanderhaeghen, Phys. Lett. B **719**, 136 (2013).
19. J. Boucher, “Feasibility studies of the $\bar{p}p \rightarrow e^+e^-\pi^0$ electromagnetic channel at PANDA”, PhD thesis, Institut für Physik, Mathematik und Informatik, Johannes Gutenberg Universität Mainz jointly with Institut de Physique Nucleaire d’Orsay, Université Paris-Sud, UMR 8608, CNRS-IN2P3, Orsay, France (2011).
20. M.C. Mora Espí, “Feasibility studies for accessing nucleon structure observables with the PANDA experiment at the future FAIR facility”, PhD thesis, Institut für Kernphysik, Johannes Gutenberg Universität Mainz, Mainz, Germany (2012).
21. S. Agostinelli *et al.* [GEANT4 Collaboration], Nucl. Instrum. Meth. A **506**, 250 (2003).
22. K. Föhl *et al.*, Nucl. Instrum. Meth. A **595**, 88 (2008).
23. M. Born and E. Wolf, “Principles of Optics”, Oxford, Pergamon (1970).
24. B. Pire, K. Semenov-Tian-Shansky and L. Szymanowski, Phys. Rev. D **84**, 074014 (2011).
25. N. G. Stefanis, Eur. Phys. J. direct C **7**, 1 (1991).
26. V. L. Chernyak, A. A. Ogloblin, I. R. Zhitnitsky, Z. Phys. C **42**, 583 (1989).
27. M. Pelizaeus, unpublished (2009).
28. A. Ryd, D. Lange, N. Kuznetsova, S. Versille, M. Rotondo, D. P. Kirkby, F. K. Wuerthwein and A. Ishikawa, “EvtGen: A Monte Carlo Generator for B-Physics” EVTGEN-V00-11-07.
29. T. C. Bacon, I. Butterworth, R. J. Miller, J. J. Phelan, R. A. Donald, D. N. Edwards, D. Howard and R. S. Moore, Phys. Rev. D **7**, 577 (1973).
30. O. Czyzewski *et al.*, Proc. of the Sienna International Conference on Elementary Particles, edited by G. Bernardini and G.P. Puppi (Società Italiana di Fisica, Bologna, Italy, 1963), p. 271 (also available as CERN/TC/PHYSICS 63-34).
31. D. Everett, P. Grossmann, P. Mason and H. Muirhead, Nucl. Phys. B **73**, 449 (1974).
32. F. Sai, S. Sakamoto and S. S. Yamamoto, Nucl. Phys. B **213**, 371 (1983).
33. A. Abele *et al.* [Crystal Barrel Collaboration], Phys. Lett. B **469**, 270 (1999).
34. J. Van de Wiele and S. Ong, Eur. Phys. J. A **46**, 291 (2010).
35. T. Ullrich and Z. Xu, (2008), arXiv:0701199v1 [physics.data-an].
36. B. Pire, K. Semenov-Tian-Shansky and L. Szymanowski, Phys. Rev. D **82**, 094030 (2010).
37. B. Pasquini, M. Pincetti and S. Boffi, Phys. Rev. D **80**, 014017 (2009).
38. A. T. Goritschnig, B. Pire and W. Schweiger, Phys. Rev. D **87**, 014017 (2013).